JGR Space Physics

RESEARCH ARTICLE
10.1029/2022JA030883

High-Latitude Plasma Convection Based on SuperDARN Observations and the Locally Divergence Free Criterion

W. A. Bristow[1], L. R. Lyons[2], Y. Nishimura[3], S. G. Shepherd[4], and E. F. Donovan[5]

[1]Pennsylvania State University, University Park, PA, USA, [2]University of California Los Angeles, Los Angeles, CA, USA, [3]Boston University, Boston, MA, USA, [4]Dartmouth College, Hanover, NH, USA, [5]University of Calgary, Calgary, AB, Canada

Key Points:

- Development of a new technique for estimating flow in the ionosphere
- The new technique provides high-resolution estimates of the flows
- The flows show good correlation with the auroral luminosity

Supporting Information:

Supporting Information may be found in the online version of this article.

Correspondence to:

W. A. Bristow,
wab5217@psu.edu

Citation:

Bristow, W. A., Lyons, L. R., Nishimura, Y., Shepherd, S. G., & Donovan, E. F. (2022). High-latitude plasma convection based on SuperDARN observations and the locally divergence free criterion. *Journal of Geophysical Research: Space Physics*, *127*, e2022JA030883. https://doi.org/10.1029/2022JA030883

Received 29 JUL 2022
Accepted 2 DEC 2022

Abstract A new technique for estimating the global-scale pattern of magnetospheric convection in the ionosphere is presented. The technique uses the Super Dual Auroral Radar Network line-of-sight velocity observations combined with an empirical convection model and the assumption that the resulting velocity field is divergence free. In contrast to other techniques for convection estimation, it does not express the velocity field in terms of known basis vectors and it does not assume that the velocity can be determined from a static potential. The velocity is estimated by applying Bayesian inverse theory to the input data, model, and constraints. Linear equations for the plasma velocity at every point in the domain are solved simultaneously in a least squares sense. Application of the technique results in convection patterns with spatial resolution equal to the calculation grid spacing. The resulting patterns conform with expectations based on the observed interplanetary magnetic field conditions and display features that show close correspondence to simultaneously observed features in the auroral luminosity.

Plain Language Summary A new technique for estimating the global-scale pattern of plasma flow in the ionosphere is presented. The technique uses radar observations from a network of radars called the Super Dual Radar Network or Super Dual Auroral Radar Network. The observations are combined with a model that gives average patterns for the conditions at the time of the observations and some assumptions about the nature of the flow velocity to produce global-scale patterns. The results will be useful for other studies of the magnetosphere, ionosphere, and upper atmosphere where understanding how the plasma moves is important.

1. Introduction

Estimating the large-scale pattern of plasma motion in the high-latitude ionosphere is necessary for understanding a number of space physics phenomena. Examples range from studies of the coupling of solar wind energy into the magnetosphere to the generation of gravity waves in the thermosphere. It is critical for studies of the dynamics of any magnetosphere-ionosphere coupling phenomena, including substorms. Global-circulation models such as the Thermosphere Ionosphere Global Circulation Model (Roble & Ridley, 1994) and the Global Ionosphere-Thermosphere Model (Ridley et al., 2006) require that the potential is specified over their entire domain for predicting evolution of the electron density structure and quantifying the transfer of energy from the plasma to the neutral atmosphere.

While the scientific need for estimating the convection pattern is clear, there is no single instrument that can provide its instantaneous measurement, which has led to the development of techniques for combining distributed local measurements to produce the large-scale pattern. The first of these techniques were based on magnetometer observations and a model for the ionospheric conductance (Kamide et al., 1981; Papitashvili et al., 1994). A number of simplifying assumptions allowed the magnetic perturbations that the magnetometers observed to be expressed in terms of a scalar magnetic potential that was determined from an ionospheric equivalent current function. The horizontal ionospheric currents were then determined from the equivalent current, and the electric fields were determined from those currents through Ohm's law and an assumed conductance pattern.

The Assimilative Mapping of Ionospheric Electrodynamics (AMIE) technique (Richmond, 1992) was a natural progression from the original magnetometer-based estimations. While still reliant on magnetometer observations, it allowed incorporation of additional data such as line-of-sight (LOS) velocities observed by radars and satellite based drift meter observations. In AMIE, the electric field in the ionosphere is expressed as a series expansion in orthogonal polynomials. The coefficients of those polynomial are determined using a technique that accounts for

the physical relationship between the observations and the electric field and that for uncertainties in the observations. Many of the techniques for convection pattern estimation developed since AMIE build upon its rigorous formulation (e.g., Cousins et al., 2013b; Matsuo et al., 2005; Ruohoniemi & Baker, 1998).

The Super Dual Auroral Radar Network (SuperDARN) was designed for the purpose of providing the observations to enable estimates of the large-scale pattern of high-latitude plasma motion over a large area as possible (Greenwald et al., 1995). The network grew out of the development of a single HF radar at Goose Bay, Labrador (Greenwald et al., 1985), which demonstrated the ability of an HF radar to observe the drift of field-aligned plasma irregularities (FAI) over a field of view that spanned a sector of more than 50°in azimuth and more than 2,000 km in range. The utility of HF radars for observing over large regions has led to the construction of more than 30 radars with fields-of-view that cover much of the high-latitude regions of both the northern and southern hemispheres. While research addressed by the network has expanded well beyond the original vision (e.g., Chisham et al., 2007; Nishitani et al., 2019), its main purpose remains estimation of the large-scale convection pattern.

SuperDARN radars observe the Doppler frequency shift caused by coherent scattering from FAI. The frequency shift translates to the projection of the plasma velocity ($\mathbf{v}$) along the radar line of sight, which is referred to as the line-of-sight velocity (v_{los}). Because the irregularities are strongly aligned with the magnetic field, only signals at normal incidence to the field direction scatter back to the radars. Hence v_{los} is due to motion in the field perpendicular direction. For radar signals scattered from F-region altitudes the FAI move with the bulk plasma velocity, which is the so-called *E-cross-B* velocity, where $\mathbf{E}$ is the electric field in the frame of reference of the measurement and $\mathbf{B}$ is the Earth's magnetic field. Usually when analyzing plasma velocity observations it is assumed that conditions are static, which means that $\mathbf{E}$ can be derived from a potential ($\mathbf{E} = -\nabla\Phi$). In this study a slightly different assumption is used. It is assumed that the velocity field is divergence free ($\nabla \cdot \boldsymbol{v} = 0$), which will be shown to encompass the static case but extends to some wave electric fields as well.

This study presents global-scale patterns of convection estimated from SuperDARN observations by solving for the velocity field directly rather than solving for a potential function. The solution does not rely on an expression of the field in terms of a series of orthogonal polynomials. Rather, linear equations for the plasma velocity at every point in the domain are solved simultaneously in a least squares sense. The system of equations expresses the velocity at each point in terms of the radar observations, the divergence free assumption, and a climatological model of the velocity.

2. Review of Techniques for Forming Convection Patterns

The most widely used technique for generation of convection patterns is to express the electrostatic potential in a finite order series expansion in spherical harmonics or similar functions. The technique used in this study is not such an expansion but the mathematical background is similar.

Richmond and Kamide (1988) (hereafter RK88) provides a discussion of the mathematical background for estimating the high-latitude potential from a collection of measurements from diverse sources. The manuscript describes what is now known as AMIE (Richmond, 1992), which combines measurements from different types of instruments (magnetometers, incoherent-scatter radars, satellite drift meters, etc.) in a mathematically rigorous manner. The technique is general and other techniques that have been employed for convection pattern estimation can be understood from it. Equation 28 of RK88 expresses a set of observations in terms of a matrix-vector product plus a residual:

$$\boldsymbol{\eta} = \mathbf{D}\mathbf{u} + \mathbf{v}, \tag{1}$$

where, $\boldsymbol{\eta}$ is a vector of observations, $\mathbf{D}$ is a matrix formed using a set of basis vectors for the data as its columns, $\mathbf{u}$ is a vector of coefficients of those basis vectors, and $\mathbf{v}$ is a residual difference between the observations and $\mathbf{D}\mathbf{u}$. The residual represents any component of the observations that cannot be expressed in terms of the basis vectors, which includes noise and nonnoise components of the observations that project into the null space of $\mathbf{D}$.

RK88 assumed that the electric field in the ionosphere, $\mathbf{E}$, can be determined from the electrostatic potential, Φ, and that other ionospheric quantities related to the measurements can be determined from $\mathbf{E}$:

$$\mathbf{E} = -\nabla\Phi, \qquad \mathbf{I}_{\mathbf{i}} = \boldsymbol{\Sigma} \cdot \mathbf{E}, \qquad J_{\|i} = \nabla \cdot \mathbf{I}_i, \tag{2}$$

where $\mathbf{I}_i$ is the horizontal current vector in the ionosphere, and $J_{\|i}$ is the field-aligned current density in the ionosphere. With these assumptions, optimizing the solution in terms of $\mathbf{E}$ provides estimates of the other quantities. Up to this point, the various techniques for estimating the high-latitude potential are essentially the same. The differences come in the choice of basis in Equation 1 and how the system is constrained so it can be inverted to provide estimates of the vector coefficients ($\hat{\mathbf{u}}$).

In RK88, all quantities (observations and fitted parameters) are expressed as the sum of an expected value and a deviation. The expected values are determined from ensemble averages, while the deviations are determined through inverting Equation 1. Elements of $\mathbf{D}$ are the values of the electric field basis functions calculated at the measurement locations. The basis functions are constructed from the gradient of Φ, which is expressed as a sum of functions of colatitude, θ, and longitude. The longitude functions are simple sinusoids while the latitude dependence is given by a piecewise continuous merging of generalized associated Legendre functions, $P_n^m(\cos\theta)$ with noninteger index n, over the range from a given colatitude θ_0 to the pole and extensions to the equator with functions that transition monotonically from $P_n^m(\cos\theta_0)$ to 0 at the equator. Note that while similar to spherical harmonics, they use noninteger index Legendre functions and are modified at latitudes below θ_0. The null space of $\mathbf{D}$ includes all basis functions of order higher than the order of the fit.

A covariance-weighted minimum-norm least squares solution was used to estimate the values of the coefficients, $\mathbf{u}$ in Equation 1. The minimum-norm constraint is essentially another assumption about the character of the high-latitude electric field that may or may not be evident in the data; however, in the case that the number fitted parameters exceeds the number of observations, some assumption is necessary to constrain the solution. Further regularization of the solution is achieved by limiting the highest order of function used to form $\mathbf{D}$. In RK88 the maximum order of the longitude functions was 10, which means the finest scales that could be represented were on the order of 1/20 of 360° in longitude and a comparable fraction of the latitude range from θ_0 to the pole.

Ruohoniemi and Baker (1998) (RB98) presents an alternative technique, SuperDARN MapPotential, for estimating high-latitude convection based on observations solely from SuperDARN. The radars of SuperDARN observe the projection (v_{los}) of the ionospheric plasma velocity, $\mathbf{v}$, along the radar look directions. In limiting the ingested observations to just v_{los}, the amount of data that can contribute during any given interval is greatly reduced from what can be used by AMIE. It does, however, provide two advantages that compensate for this limitation. First, since the v_{los} are derived from coherent-scatter radar observations, the detected velocity component is in the direction perpendicular to the magnetic field, $\mathbf{B}$. This feature eliminates the need to assume a value for the field-aligned component of the velocity as is required when using observations from incoherent-scatter radars. Second, it is not necessary to assume a conductivity model, which is required when using magnetometer observations. This aspect is a significant advantage because mesoscale features associated with auroral features are not present in conductivity models.

RB98 follows the technique of RK88 for expressing the $\mathbf{E}$ as the gradient of a scalar potential and expands that potential in a series of functions. They use the spherical harmonics without modification; however, they modify the latitude variable to constrain the domain to the region above a low-latitude limit, Λ_0, which was a circle of constant latitude. In a later study using the technique described in Shepherd and Ruohoniemi (2000) Λ_0 was replace by Λ^{HMB} which varies with longitude to resemble the boundary defined by Heppner and Maynard (1987). To estimate the coefficients of the expansion, MapPotential uses a variance-weighted least squares solution that minimizes the squared-difference between the observed v_{los} and the projection of the $\mathbf{E} \times \mathbf{B}$ velocity along the radar lines of site with the additional constraint that in regions where no observations are available, an empirical convection model is used. The number of model sample points is based on the order of the fit and is chosen to stabilize the solution while minimizing the influence of the model. The model (Ruohoniemi & Greenwald, 1996) was based on long-term averages of the SuperDARN observations binned by prevailing interplanetary magnetic field (IMF) and solar wind (v_{sw}) conditions. Current versions of the MapPotential software allow a choice of empirical model from a number that have been developed over the years (Cousins & Shepherd, 2010; Pettigrew et al., 2010; Thomas & Shepherd, 2018). With similar fit orders as employed in AMIE, similar resolution is achieved. However, because MapPotential does not apply the minimum-norm constraint, the solutions often exhibit more structure than appears in patterns from AMIE.

Cousins et al. (2013b) describe another potential estimation technique, SuperDARN assimilative mapping (SAM), that warrants discussion. SAM is similar to both of the other techniques but with some unique features. First, like RB98 the assimilation uses only SuperDARN v_{los} data so has advantages and disadvantages discussed above.

Likewise, it samples an empirical model based on SuperDARN observations to give the average state. It follows a similar formulation of RK88 to determine deviations from the average state and seeks a minimum norm solution. The main unique feature of SAM is in its choice of empirical orthogonal functions (EOFs) as basis functions (Cousins et al., 2013a). The EOFs are derived from SuperDARN data to represent the dominant modes of variability in convection patterns. The individual EOFs are represented in terms of the basis functions used in RK88 to an order of 12, which yields a resolution of 2.5° in latitude and 15° in longitude in each function. The patterns generated by SAM typically show less structure than those generated by MapPotential. In cross validation tests (Cousins et al., 2013b), SAM produced significantly smaller errors than MapPotential when predicting a data test set, and the values of cross-polar-cap potential predicted by SAM were generally higher than those predicted by MapPotential. Recent work by Matsuo et al. (2021) builds on the SAM technique by adding a needlet-based random electric field model to SAM patterns in an attempt to better characterize small-scale variability.

Like these studies, the technique presented here provides estimates of the high-latitude convection pattern based on a set of distributed observations. It relies on the SuperDARN v_{los} alone but could ingest other observations with minor modifications. It uses an empirical model in addition to the observations. In contrast to the other techniques, it does not express the matrix $\boldsymbol{D}$ in terms of known basis vectors and it does not assume that the velocity can be determined from a static potential. The only explicit assumptions are (a) that the v_{los} are projections of the field-perpendicular velocities, $\mathbf{v}$, along the radar look directions and (b) that the velocity field is divergence free, $\nabla \cdot \boldsymbol{v} = \boldsymbol{0}$. Added to these, there is the implicit assumption that the empirical model selected from a set of key parameters is representative of the convection within the uncertainty of the model. The mathematical details of determining a velocity field from these assumptions are given in Bristow et al. (2016). In that paper, the technique was referred to as Local Divergence Free Fitting (LDFF) since it provided individual vectors based on local quantities rather than a global potential. Here the LDFF technique is extended to provide similar local vectors but over global-scale regions. The velocities are determined by minimizing the residuals in local equations over a global-scale region, so we will refer to it as the Global, Local Divergence Free Fitting (G-LDFF) technique.

3. Divergence Free Criterion

As long as the plasma is frozen to the magnetic field, the divergence free flow criterion is equivalent to saying that the magnetic flux in the ionosphere is incompressible. As has been pointed out by others (Kivelson & Southwood, 1991; Lockwood & Morley, 2004), the Alfvén speed in the ionosphere ($\sim 10^5$ m/s) greatly exceeds both the sound speed and the highest flow speeds (both $\sim 10^3$ m/s), which means that any localized perturbations to the field are communicated away at the Alfvén speed. For any time that is long compared to the Alfvén time ($\tau_A = d/v_A$), which for $d = 100$ km is less than a second, compressions of the field can be ignored. The G-LDFF technique applies the divergence free condition locally at the grid-cell level over the entire high-latitude region, on a timescale of about a minute. With the 100 and 50 km grid cells used in this study any deviation from incompressibility should be negligible.

The assumption that the velocity field is divergence free encompasses the case of static fields but perhaps is more general since it can include some time varying conditions. To illustrate this point, it is assumed that the velocity is the $\mathbf{E} \times \mathbf{B}$ velocity then,

$$\begin{aligned} \nabla \cdot \boldsymbol{v} &= \nabla \cdot \left(\mathbf{E} \times \mathbf{B} / B^2 \right) \\ &= \nabla \left(\frac{1}{B^2} \right) \cdot (\mathbf{E} \times \mathbf{B}) + \frac{1}{B^2} \nabla \cdot (\mathbf{E} \times \mathbf{B}) . \end{aligned} \tag{3}$$

Assuming that gradient of the magnitude of $\mathbf{B}$ is small compared to the other terms, the first term on the right hand side of Equation 3 can be neglected. In the second term, assume the magnetic field includes the Earth's main field plus contributions from static currents and a wave perturbation to get the following equation:

$$\begin{aligned} \nabla \cdot \boldsymbol{v} &\approx \frac{1}{B^2} \nabla \cdot (\mathbf{E} \times \mathbf{B}) \\ &= \frac{1}{B^2} \mathbf{B} \cdot (\nabla \times \mathbf{E}) - \frac{1}{B^2} \mathbf{E} \cdot (\nabla \times \mathbf{B}) \\ &= \frac{1}{B^2} \mathbf{B} \cdot \frac{\partial \mathbf{B}}{\partial t} - \frac{\mathbf{E} \cdot \mathbf{J}}{B^2 / \mu_0} \end{aligned} \tag{4}$$

where μ_0 is the permeability of free space. The first term on the right hand side of Equation 4 would vanish whenever the perturbation component is perpendicular to **B**, which is true for shear Alfvén waves. Further, the magnitude of the term is the rate of change of B (at most $\sim 100's$ of nT/s) divided by the magnitude of B, which is on the order of $25 - 50$ μT. Hence the ratio will be less than ~ 0.004 s^{-1} for all perturbations. The second term is the ratio between Joule dissipation and the energy density in the main field. At the lowest values of the main field (25 μT), the energy density is about 0.5 mJ/m^3. With electric fields in the range of 10–100 mV/m and F-region Pedersen conductivities of a few times 10^{-5} S/m, the Joule dissipation power density is on the order of (50 mV/m)^2(5×10^{-5} S/m) = 1.25 μW/m^3. Hence, the ratio of the dissipation to the main field energy density would be on the order of 0.00025 m/s/m. In the numerical solution for the convection pattern in terms of a system of linear equations, the divergence is calculated over the size of a grid cell. With a 50 km grid size (typical range resolution of SuperDARN) this ratio would give a velocity difference of 12.5 m/s across a cell. While this value is not zero, it is small compared to other terms in the set of equations. For example, in a region where the electric field was 50 mV/m, the velocity would be on the order of 1,500 m/s and the projection onto the radar look directions would be of the same order. Hence, setting the divergence value to zero and using a small nonzero uncertainty in the least squares solution is justified.

As a side note, since dissipation appears in Equation 4, it is worth revisiting the assumption of the frozen in condition, that is, the $\mathbf{E} \times \mathbf{B}$ velocity. In an Appendix A, it is shown that in the presence of small dissipation the divergence of the velocity is modified to be

$$\nabla \cdot \mathbf{v} = \frac{1}{\nu^2/\Omega^2 + 1} \frac{1}{B^2} \nabla \cdot (\mathbf{E} \times \mathbf{B}) + \frac{q\nu/m}{\nu^2 + \Omega^2} \nabla \cdot \mathbf{E} \tag{5}$$

The first term is similar to Equation 3 but is reduced by a small factor. The proportionality in the denominator is the square of the ratio of the ion-neutral collision frequency (ν) to the ion gyro frequency (Ω). Recent rocket-based measurements show the ratio (Sangalli et al., 2009) to be about 1/10 in the upper E-region. With the exponential decrease in neutral density and the transition to oxygen ions, the F-region ratio would be significantly lower. The second term is the product of the ion Pedersen mobility and the divergence of **E**, which is charge density. Over the timescales and length scales of interest, any charge accumulation would be negligible.

4. Global-Scale Bayesian Inverse

In Bayesian estimation, some desired model quantities are determined by inverting a system of equations relating the model to a set of observations along with any equations of constraint and prior information. Here, the desired model quantities are the plasma velocities ($\{\mathbf{v}_i\}$) at a set of locations. The system of equations is the set formed by combining the projection of the plasma velocity along the radar lines of sight $\left(v_{los} = \mathbf{v} \cdot \hat{k}\right)$ in every grid cell where an observation is available, along with the divergence-free field property as a constraint and a climatological model of the velocity field ($\{\bar{\mathbf{v}}_i\}$) as assumed as prior information.

Bristow et al. (2016) presented the technique for obtaining regional estimates of the plasma velocity field with a spatial resolution that was comparable to the resolution of the v_{los} observations. The technique was a two-step process in which the SuperDARN v_{los} observations were used first in the MapPotential technique to calculate an estimate of a background field and then a used second time in a Bayesian inversion to get the local velocity estimates.

In the work presented here, the initial step of using MapPotential to get the low-resolution background was replaced by sampling a climatological model that provides estimates of the velocity and its variance at every grid point in the domain of the calculation. The model (Bristow et al., 2022) (hereafter ML-model) is based on using SuperDARN observations from 4 years (2014–2017 inclusive) to train a machine learning model. The training database consisted of convection patterns formed using the standard SuperDARN RB98 algorithm. The model is keyed to the IMF and solar wind velocity, but also uses the auroral indices AL and AU, and the global index *SYM-H* to capture the variability of convection driven by the internal magnetospheric state. The model has a resolution of 1-hr in MLT and 2° in magnetic latitude between 55° and the magnetic pole. Model values were linearly interpolated between the model grid points to get the values at the calculation grid points used here.

Figure 1 shows an example ML-model pattern for southward IMF of about 5 nT and AU and AL magnitudes of greater than 100 nT.

The ML-model was used because of its ability to capture the convection patterns dependence on the internal magnetospheric state. With this dependence, the latitude of the convection reversal boundary and strength of convection respond to changes of the AU, AL, and SYM/H parameters. In comparisons to a previous convection model (Thomas & Shepherd, 2018), the ML-model showed significantly lower root-mean-squared error when predicting a set of test data (Bristow et al., 2022).

The grid for convection pattern estimation was chosen to provide moderate spatial resolution (~100 × 100 km) over the entire domain but has the option of including a nested-grid region with cells of half the dimensions (~50 × 50 km) of the main grid. This nested region provides similar resolution to that of the regional patterns described in Bristow et al. (2016). The reason for not simply using the finer grid over the entire domain is that the computational cost increases with at least the square of the number of grid cells so the factor of four increase in number of grid cells would translate in to at least a factor of 16 increase in computation time. The version of the code used to analyze the data in this manuscript requires about 40 s per time step on a recent model desktop computer when using a nested grid that covers about 20° of latitude and 100° of longitude for a total grid of just over 6,000 points. Further, there is no reason to use the fine grid where there are not any observations because the results will revert to ML-model resolution in those regions.

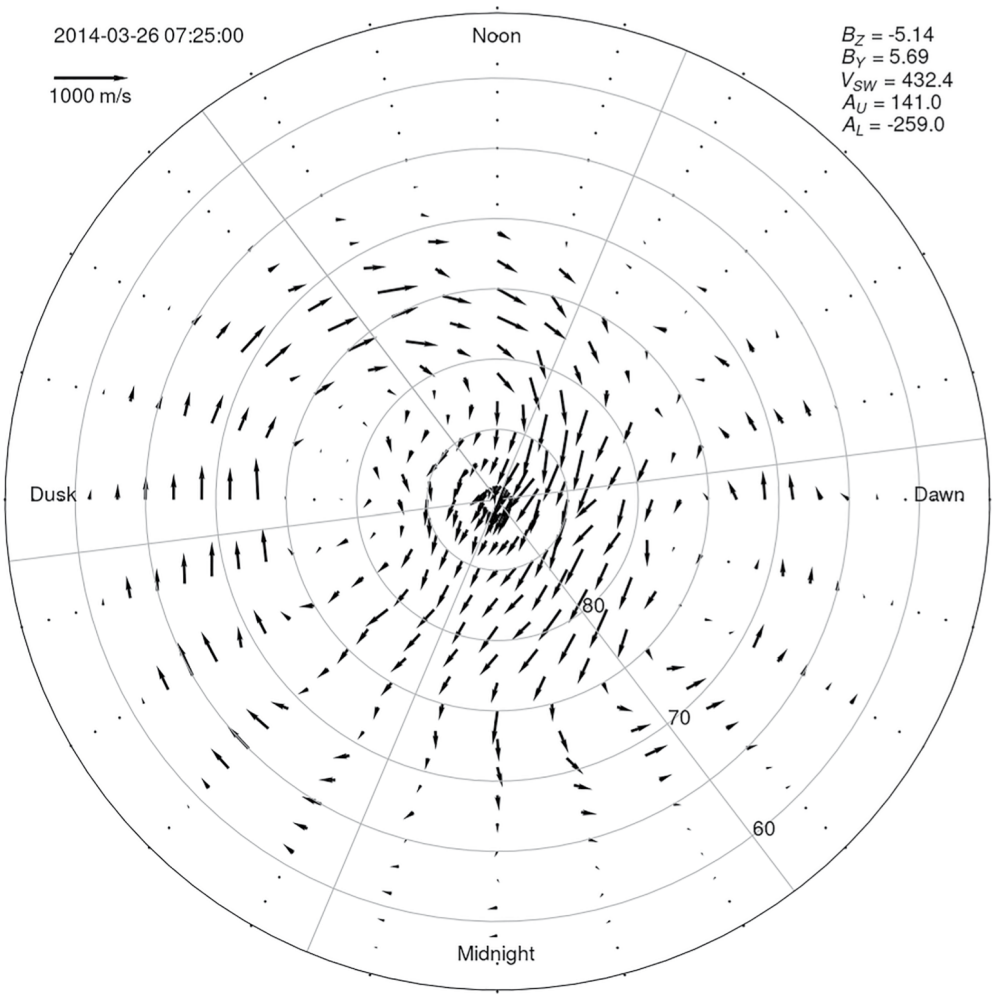

Figure 1. Output of the machine learning based empirical convection model displayed on the latitude-MLT grid for $B_z = -5.14$ nT, $B_y = 5.69$ nT, AU = 141 nT, and AL = −259 nT.

As in the previous work we write the system of equations constraining the estimation as $\mathbf{Gm} = \mathbf{d}$, with the elements given by the following equation:

$$\begin{bmatrix} \sin\theta_{b11} & 0 & \dots & \cos\theta_{b11} & 0 & \dots & \dots \\ 0 & \sin\theta_{b12} & \dots & 0 & \cos\theta_{b12} & \dots & \dots \\ \vdots & & & & & & \\ \frac{-1}{\Delta e} & \frac{1}{\Delta e} & \dots & \frac{-1}{\Delta n} & \dots & \frac{1}{\Delta n} & \dots \\ \vdots & & & & & & \\ 1 & 0 & \dots & 0 & \dots & \dots & \dots \\ 0 & 0 & \dots & 1 & \dots & \dots & \dots \end{bmatrix} \begin{bmatrix} v_{e12} \\ v_{e12} \\ \vdots \\ v_{n11} \\ v_{n12} \\ \vdots \end{bmatrix} = \begin{bmatrix} v_{\text{los}11} \\ v_{\text{los}12} \\ \vdots \\ 0 \\ \vdots \\ \tilde{v}_{e11} \\ \tilde{v}_{n11} \end{bmatrix} \tag{6}$$

The first block of rows in $\mathbf{G}$ give the projection operation along the beam directions, followed by rows to express the divergence operation, and finally followed by the specification of the velocity from the ML-model. The corresponding elements of the vector $\mathbf{d}$ give the LOS observations, zeroes for the value of the divergence at each grid point, and the values from the ML-model velocity indicated by the components with the tilde overbar.

Each element of the vector $\mathbf{d}$ has an associated uncertainty, which corresponds to the variance of the probability distribution from which it was drawn. The uncertainty in each v_{los} is provided in the SuperDARN data files. For the ML-model, the mean-squared difference between model predictions and corresponding values in its test set were used. These values were interpolated from the ML-model grid to the computational grid in the same way as the ML-model velocities. The uncertainty in the divergence free condition does not have a clearly defined value that comes from the theory. It does, however, play a significant role in determining the character of the resulting convection patterns. The value was set to be 0.01 $(\text{m/s/m})^2$, which was chosen by trying inversion using a number of values and examining the resulting patterns and the differences between the input v_{los} and the projections of the results onto the radar look directions. It was found that if the divergence value was higher, the resulting convection patterns exhibited discontinuities between the regions of observations and regions outside the observations. If the uncertainty value was lower, the patterns appeared overly smoothed and under emphasized the observations in comparison to the ML-model. The value can be viewed as a tuning parameter similar to the fit order used in functional expansions. The uncertainties were used as the diagonal elements of the matrix $\mathbf{C_d}$, which was used in inversion of Equation 6.

Equation 6 is inverted to obtain the estimated velocities using a standard weighted least squares solution:

$$\mathbf{m} = \left[\mathbf{G}^{\mathsf{T}}\mathbf{C}_{\mathbf{d}}^{-1}\mathbf{G}\right]^{-1}\mathbf{G}^{\mathsf{T}}\mathbf{C}_{\mathbf{d}}^{-1}d. \tag{7}$$

Because the matrix $\mathbf{C_d}$ is diagonal, its inverse is simply a matrix with the reciprocal of the diagonal elements. In the implementation of the algorithm used to produce the results presented here, the inverse in the matrix in brackets was found using conjugate-gradient-least squares (CGLS) (Hestenes & Stiefel, 1952), which is an iterative algorithm for finding least squares solutions to systems of linear equations. CGLS is a Krylov subspace method, which means that the solution can be decomposed into a set of basis vectors that are generated from products of powers of the coefficient matrix $\left(\mathbf{G}^{\mathbf{n}}\right)$ with the data vector $(\mathbf{d})$. The method is efficient in that the only operations in the iteration are matrix-vector products and additions. The iteration is stopped based on the tolerance for the magnitude of some residual norm, which is typically chosen to be $\|\mathbf{Gm} - \mathbf{d}\|_2^2 < \delta$. In our implementation, the condition for terminating the iteration was

$$\frac{\|\mathbf{Gm} - \mathbf{d}\|_\infty}{\|\mathbf{d}\|_2} < \delta, \tag{8}$$

where δ is a small number. This form for the termination condition minimizes the error locally while simultaneously yielding a low global residual.

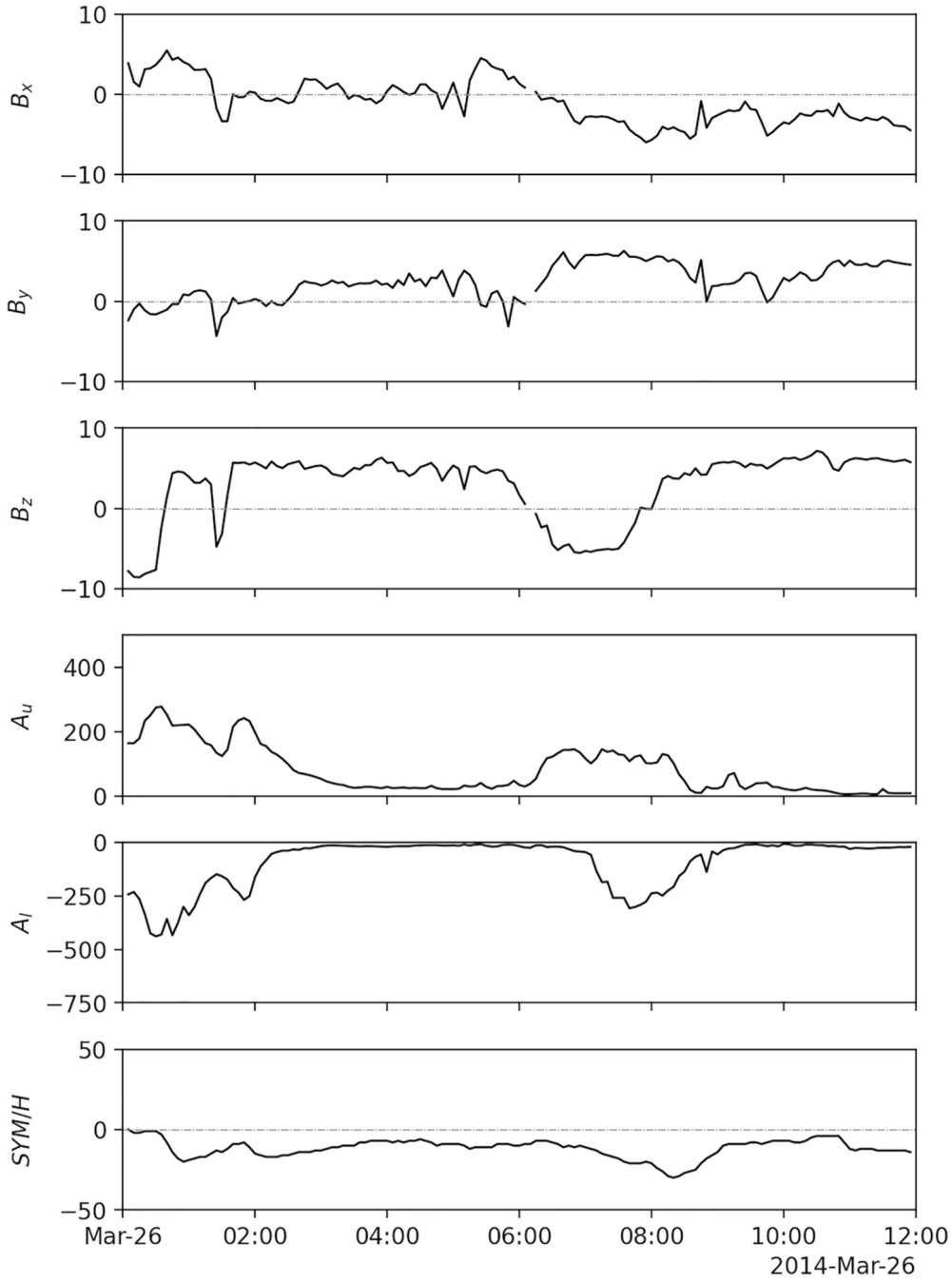

Figure 2. Observed interplanetary magnetic field and magnetic indices AU, AL, and SYM/H taken from the NASA OMNI database for the day 26 March 2014.

5. Results

To illustrate application of this algorithm, convection patterns were calculated for the day of 26 March 2014. The IMF and magnetic indices AU, AL, and SYM/H for the day are plotted in Figure 2. The data for the figure come from the NASA OMNI database (King & Papitashvili, 2005), which provides the IMF parameters aligned in time to reflect solar wind propagation delays from the point of observation to the Earth's bow shock. The figure shows that the IMF was steadily northward for most of the period from 0200 UT to 0530 UT, after which it turned southward for a period of about an hour. The AL panel shows rapid decrease of the index from about −50 nT to about

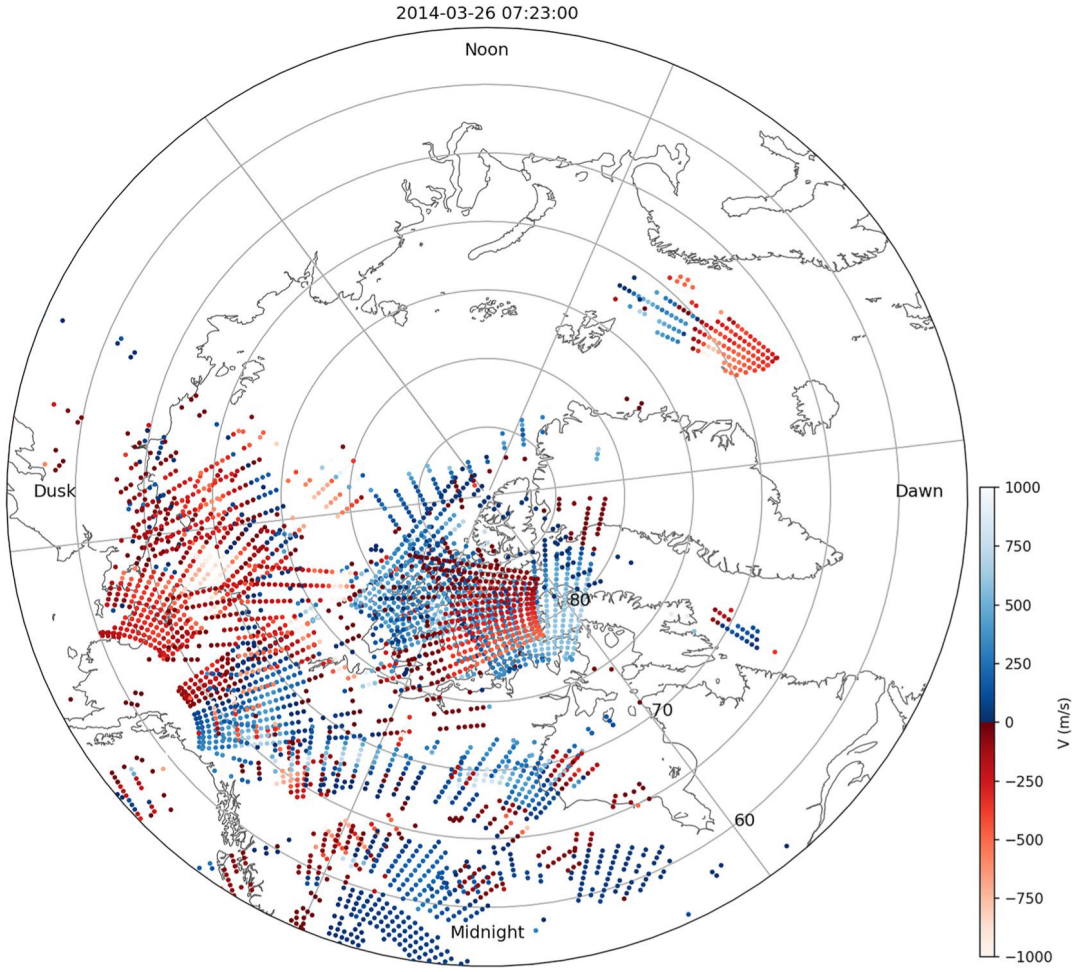

Figure 3. Velocities observed by the northern hemisphere Super Dual Auroral Radar Network radars for the two-minute interval at 0723 UT on 26 March 2014. The data are plotted in Altitude Adjusted Corrected Geomagnetic Coordinates. The interplanetary magnetic field and auroral indices from the time of the plot are given in the upper right.

−260 nT over the period from 0705 UT to 0723 UT, which may be evidence of a small substorm at that time (for an examination of the event see Lyons et al. (2019)).

Many of the northern hemisphere SuperDARN radars had nearly continuous observations throughout the period so the patterns are well constrained by observations in the North American sector. To illustrate the data coverage, Figure 3 shows v_{los} observed in the two-minute interval starting at 0723 UT plotted in Altitude Adjusted Corrected Geomagnetic Coordinates (AACGM-V2) (Shepherd, 2014) from latitude 55° to the pole. The figure illustrates that overlapping observations from multiple radars were available over the region from central Canada through western Alaska. The time of the plot coincided with the minimum of the rapid decrease in AL shown in Figure 2. At the time, North America was in the midnight sector so the array was well positioned to characterize flows in the region of the substorm onset.

Figure 4 shows the flow vectors calculated for the time shown in Figure 3 using all observations collected in the two-minute interval. Over the majority of the domain, the grid resolution was 1°in latitude. To get roughly square grid cells throughout the domain, the step in longitude was 1°divided by the cosine of the latitude. A nested grid region with half that grid spacing in both latitude and longitude covers the region from 58°magnetic latitude to 80°magnetic latitude from western Alaska through central Canada. At the time of the plot the IMF z-component was negative at ∼5 nT, with a positive y-component of comparable magnitude. The colored vectors indicate the locations where the v_{los} were available, while the gray vectors indicate locations without observation. At those locations, the velocity is determined from the fit to the ML-model combined with the divergence-free constraint.

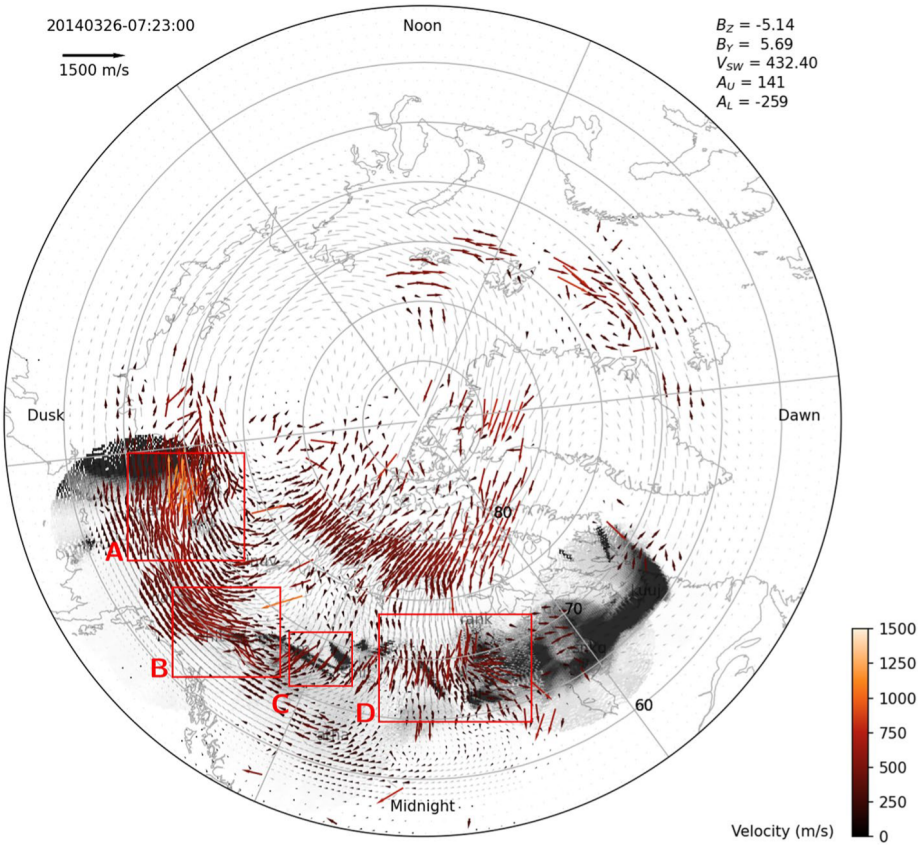

Figure 4. Convection map for 0723 UT on the day 26 March 2014. Colored vectors indicate the locations where v_{los} observations contributed to a fit. Light gray vectors indicate locations where there were no observations. Auroral luminosity observed by the THEMIS ground array is plotted in grayscale in the background. The red boxes on the plot indicate regions that are discussed in the text.

The vectors are plotted over the auroral luminosity observed by the THEMIS ground-based array, which is shown in grayscale. Dark gray corresponds to regions of bright aurora except for the region in western Alaska, which shows the brightness from the twilight. In the region without significant number of observations, the flow lines are smooth and closely resemble those in Figure 1. The vectors are significantly more structured in the regions where radar returns were observed. They show higher velocities and small-scale features not present in the ML-model. The pattern near midnight shows structure that appears closely related to the auroral luminosity.

The map in Figure 4 shows flow across the polar cap from the dayside to the nightside with a dawn-to-dusk component consistent with the observed positive IMF y-component, which is also reflected in the dayside flow entering the polar cap in the prenoon hours. Box A encloses a region where velocities were in excess of 1,000 m/s in the dusk local time sector. Flow velocities in this area were under 500 m/s in the period before the substorm onset and showed a gradual increase as the expansion began and moved westward. Box B indicates a region where the premidnight flows are parallel to the auroral arcs. The arcs and the flows are aligned primarily east-west but the arcs have a north-east to south-west tilt, which is reflected in an equatorward component of the flow velocity. In Box C, the arcs are aligned east-west but the flow velocity is essentially equatorward and perpendicular to the arcs. At the time of the frame, the arcs in this region were moving equatorward with the flow. In Box D, the aurora in the western portion was aligned north-west to south-east and turned to being east-west aligned at about the center of the box. The flow vectors in the box show a pattern that largely parallels the arcs. A video for the interval from 0600 UT to 0900 UT is available in the Supporting Information S1. The video illustrates the close association between the flow pattern and the development of the auroral arcs (Movies S1 and S2).

To better illustrate the development of the flow velocities and their association with the aurora, Figure 5 shows a sequence of images covering the period from 0643 UT to 0751 UT, which includes the time from the southward

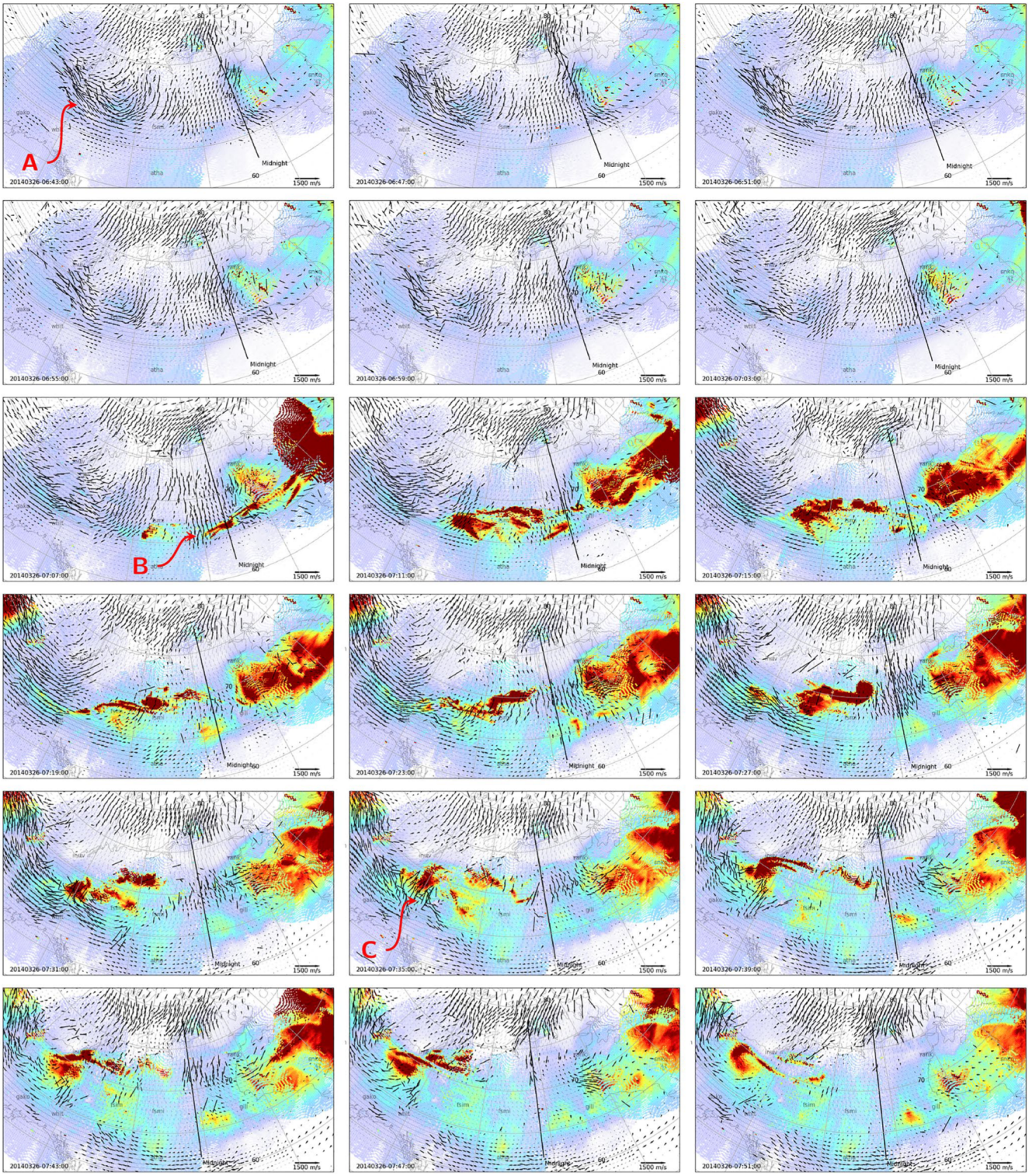

Figure 5. Sequence of convection maps for the region over North America with auroral luminosity in false color in the background. The figure covers the interval from 0643 UT to 0751 UT on 26 March 2014. Individual frames are separated by 4 min.

turning of the IMF through the substorm onset and expansion. The individual frames of the figure represent two-minute intervals and are separated by 4 min. Substorm onset, determined from the initial brightening and decrease of AL, occurred at about 0703 UT. In the first six frames, the premidnight return flow region (marked

with the letter A) and auroral arcs moved equatorward from about 70°magnetic latitude to about 65°magnetic latitude. The flow velocities in the region were in the range of 500–800 m/s throughout the period. Postmidnight flows were of similar magnitude but did not illustrate the same equatorward motion. By 0707 UT the brightening near midnight was clearly evident and had begun to expand westward. Flow at midnight at the latitude of the aurora was directed equatorward with approximately double the magnitude compared to the previous frames. The highest flow velocities appeared in a narrow channel (marked with the letter B) at a longitude just before local midnight in a region between bright arcs. In the regions dawnward and duskward of the brightening, the flow was still aligned east-west but was showing more structure than it had prior to the onset. By 0711 UT, the entire region from about 2200 MLT through midnight was filled with aurora and the flow appeared to divert away from the region and toward dusk. The aurora expanded westward, eastward, and poleward over the remainder of the interval. The location and magnitude of the flows showed a strong correlation with the aurora. At 0731 UT at a local time of about 2200 MLT, a channel of high-speed poleward flow (marked with the letter C) appeared and persisted until about 0747 UT. The channel corresponded to a significant brightening of the aurora at that local time and the subsequent rapid poleward motion of the arcs. When the poleward flow channel dissipated, the arcs stopped their poleward motion. Over the 11-minute period of the flow channel, the arcs moved from about 67° magnetic latitude to about 72° magnetic latitude, a distance of about 550 km. That motion translates to an average velocity of just over 830 m/s, which corresponds well with the observed flow velocities.

6. Discussion

Mapping convection in the ionosphere based on ground-based observations enables monitoring the state of magnetosphere and magnetosphere-ionosphere coupling. The time series of convection patterns reveal the evolution of the magnetosphere in response to external drivers and internal processes. Techniques for estimation of the pattern have evolved over recent decades with development of observational infrastructure and analysis techniques. The technique presented here represents a step in this evolution with a focus on providing better spatial resolution and better fidelity in regions where observations are available than has been achieved using global potential mapping techniques.

The correspondence of estimated flow velocities and features of the aurora illustrated in Figures 4 and 5 align with expectations based upon theory (e.g., Lysak, 1985) and observation (e.g., Burke et al., 1980). In particular, recent studies examining the association between auroral morphology and mesoscale convection features such as flow channels (e.g., Gallardo-Lacourt et al., 2014; Lyons et al., 2022) illustrate a similar correspondence between flow and aurora to the observations presented here. One of the limitations of globally regularized estimates of convection flows, such as limited order functional expansions, is their inability to provide an accurate representation of mesoscale features. The G-LDFF convection estimates provide this ability and should be useful for studies focused on auroral electrodynamics.

The G-LDFF technique presented here differs from the potential mapping techniques in several ways. One significant difference is that in regions without observations, the result will more closely resemble the background climatology than would be the case for the potential maps. The reason for this difference is that the potential mapping techniques represent the potential as a sum of a set of global basis functions with the coefficients of the sum determined from fitting. The contribution of any given function is global even if the support for it in the observations comes from a small region. In the G-LDFF technique, the influence of observations on regions outside of their extent decreases with distance through the divergence calculation. The distance over which the influence decreases depends on the assumed variance of the divergence used in the fit. It is not obvious which technique is better able to represent convection in regions away from observations. Clearly, if observed flow velocities within an isolated region differ significantly from the climatological model then it is likely that they differ elsewhere. It is not clear, however, that the functional form of a given basis function will capture that difference accurately. Perhaps the EOFs used by the SAM technique (Cousins et al., 2013b) provide the highest likelihood of representing global-scale convection since they were determined from convection observations rather than an arbitrary functional form.

Another significant difference between techniques is that, as the name implies, potential mapping provides an estimate of the potential, which can be used directly by numerical ionospheric simulation models. The models use the potential to calculate the plasma velocity as a function of altitude at every point in their domain. Because models are configured to use a potential, the G-LDFF results cannot be used directly. Calculating potential patterns from

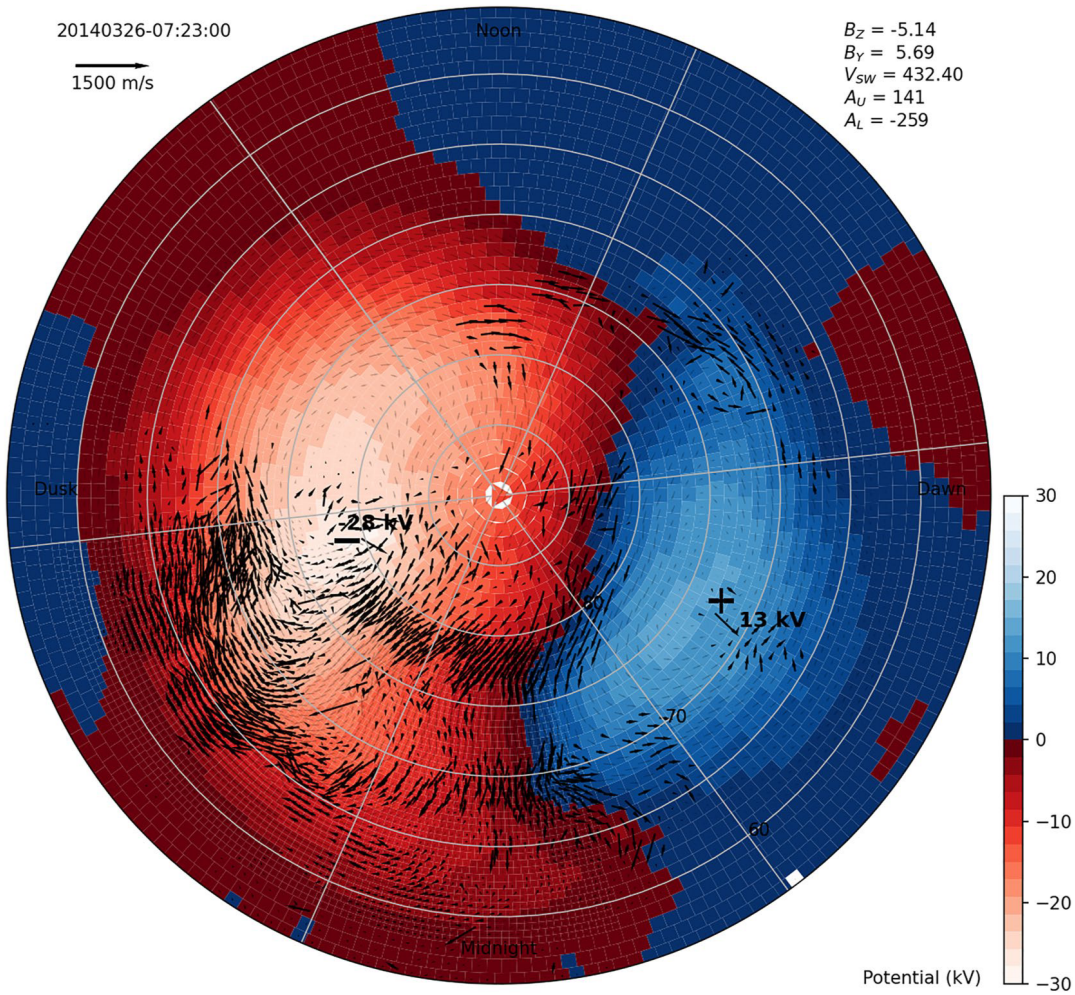

Figure 6. Electrostatic potential calculated from the Global, Local Divergence Free Fitting velocity estimate for 0723 UT on 26 March 2014.

the G-LDFF patterns is rather straight forward. First, the potential is assumed to be zero at the low-latitude boundary of the grid. The electric field (**E**) is determined by assuming that the velocity is the E-cross-B velocity. The potential could be determined from the line integral of **E** from a reference point; however, because of the variance of the fitted velocities the resulting potential depends on what path is used in the integral. To overcome this issue, it is possible to write the electric field as the numerical gradient of the potential ($\mathbf{E} = -\nabla\Phi$) at every point in the grid, which results in a set of linear equations that can be inverted to provide the potential. Figure 6 shows the potential calculated using this method for the time interval shown in Figure 4. The potential shows smooth contours in the regions where the velocity was determined by the ML-model and somewhat steeper gradients in the regions where there were observations as is illustrated by the dusk-cell minimum occurring in the region of observations.

For comparison, Figure 7 shows the potential and flow vectors estimated using the SuperDARN MapPotential technique. There are some noticeable differences between the patterns given by the two techniques. The pattern given by MapPotential is significantly smoother than that given by G-LDFF, as indicated by the velocity vectors. The point-to-point variability of the velocity vectors is much larger in the G-LDFF pattern. The MapPotential vectors are constrained to lie along the potential contours, which are smooth functions of position. The contours are determined from a finite order expansion in spherical harmonics, which oscillate in both latitude and longitude. The fit order used to produce the map in Figure 7 was eight, which means that the contours can have at most eight oscillations in latitude and in longitude over the domain. The oscillatory character of the solution is visible in the longitudinal variation of the potential contours at 80° magnetic latitude. Multiple oscillations are clearly

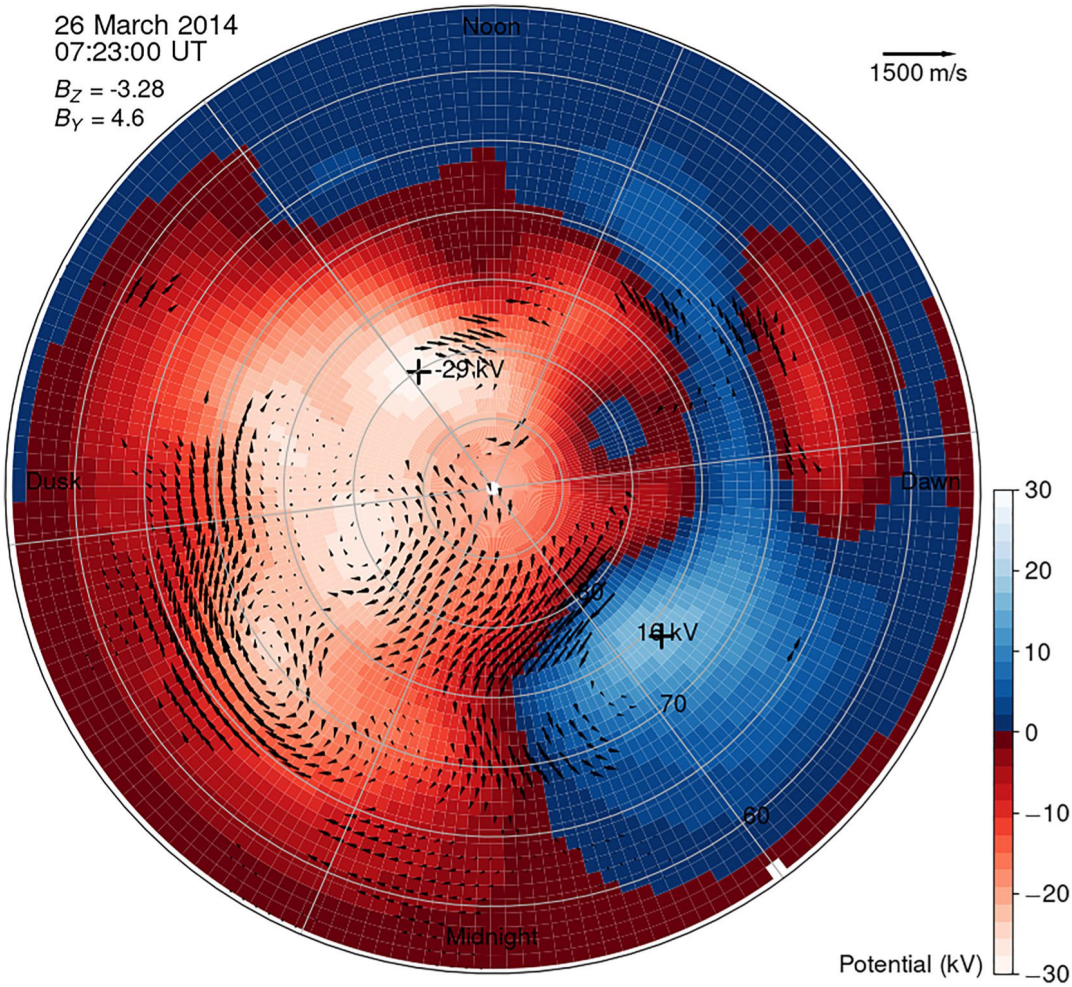

Figure 7. Electrostatic potential calculated by the Super Dual Auroral Radar Network MapPotential technique for 0723 UT on 26 March 2014.

visible in the regions where there is no data coverage. In the regions with data coverage, the oscillations result in the appearance of flow vortices, which do not appear in the G-LDFF result.

It's also worth noting that the velocities determined by the G-LDFF in Figure 6 are somewhat larger than those determined by MapPotential. It is likely that this difference comes because the global nature of the MapPotential solution would tend to damp local peaks and valleys. Hence, the highest high velocities and the lowest low velocities would be suppressed, which is not the case for the local solution of the G-LDFF.

When considering a new analysis technique it is important to evaluate how well it estimates the desired quantities. Unfortunately, there is no definitive set of convection patterns that can be considered a standard for comparison against. In such a case, a measure that is often used is to compare the original input data to values that would be predicted from the final analyzed product. Here, the input data are the v_{los}, which can be compared to the projection of the estimated velocities along the radar lines of sight. Figure 8 shows such a comparison in an overlay of three sets of vectors for the convection pattern at the time shown in Figure 4. The black vectors are the estimated velocities at the locations of observations, the teal vectors are the input v_{los}, and the red vectors are the velocity projections, which are plotted over the teal vectors. In locations where the teal is visible, the projected velocity is lower in magnitude than the input v_{los}. In locations where there is a high density of observations, there is very little teal visible, which shows that the data are dominating the solution in those regions. In regions with isolated observation points or where individual observations show a large variance from neighboring observations, there are significant differences between the data and the projections. Figure 9 shows a scatter plot of the velocity projections versus the corresponding v_{los} for the full day of 26 March 2014. In the figure, the color contours

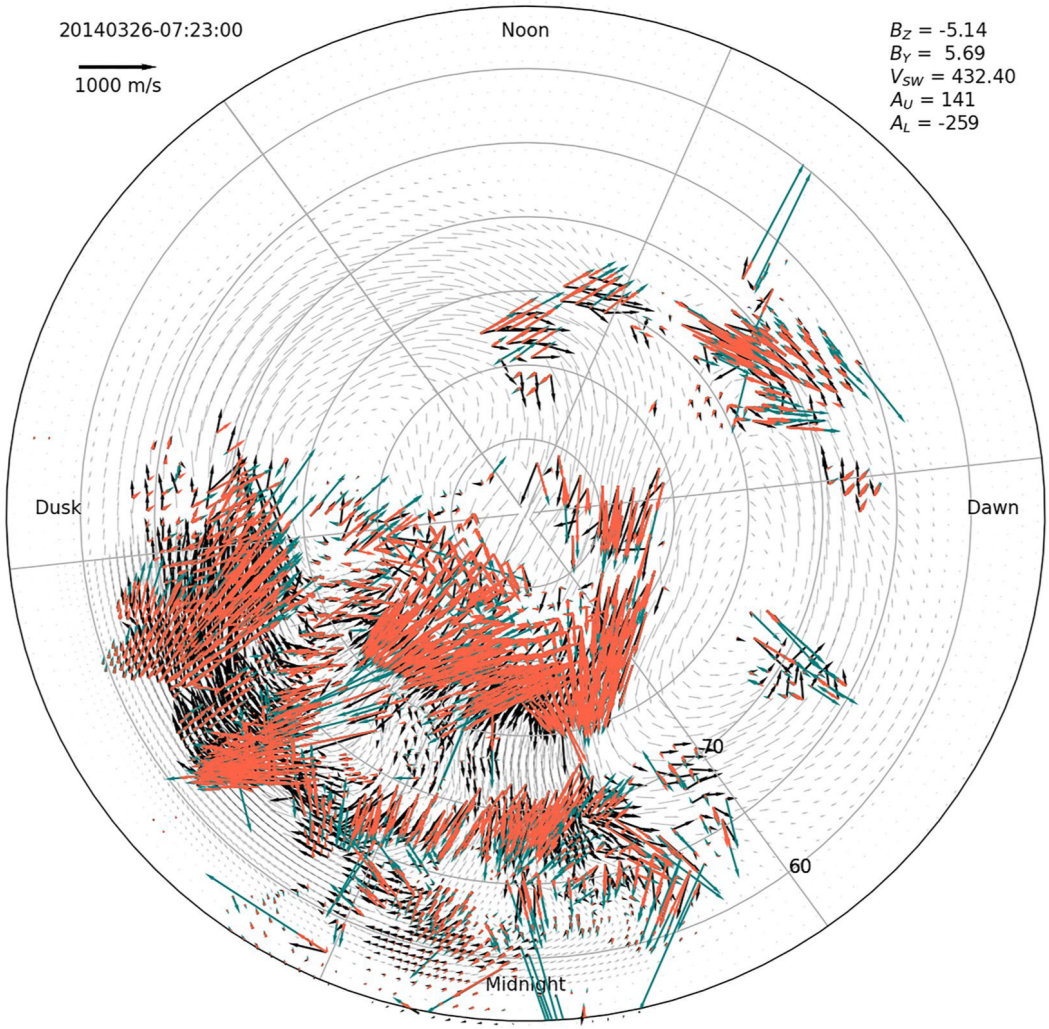

Figure 8. Convection velocities (black), v_{los} input (teal), and projections of velocities along radar lines of sight (red) for 0723 UT on 26 March 2014.

represent the density of points. There are three lines on the plot for reference: a dashed black line that shows equality ($v_{proj} = v_{los}$), a red line showing a linear fit to all of the points, and a green line that was determined by fitting to the peaks of the color contours. The color contours show that the vast majority of the points in the distribution lie quite close to the equality line. There is a tendency for the velocity projection to underestimate the v_{los}; however, the underestimation is ~50 m/s at v_{los} = 750 m/s, and smaller for smaller v_{los}. The green line, which aligns with the ridge of the distribution has a slope of about 0.94. Figure 10 shows the distribution of differences between the projections and the observations for the data shown in Figure 9. The distribution appears symmetric about a 0 difference and has a full-width at half-maximum of 50 m/s.

The combination of this analysis with the close correspondence between flow velocity features and features in the aurora provide confidence that the method provides accurate convection estimates.

As is true for any linear regression based technique, the G-LDFF technique tends to smooth out extrema. This tendency is illustrated clearly by Figures 8 and 9. The v_{los} input data that are not covered by the projections of the resolved vectors along the lines of sight are a result of this smoothing. The smoothing is a result of regularization of the solution, which is necessary whenever observations are contaminated by noise. A technique without regularization that exactly reproduced extreme data values would also reproduce or even amplify noise.

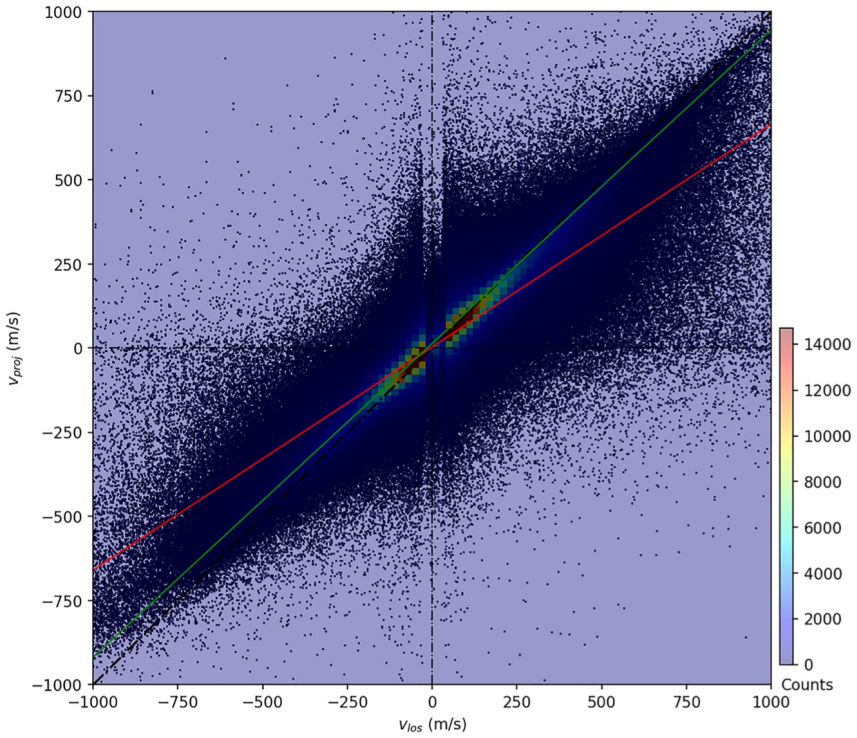

Figure 9. Scatter plot and density of projections of velocities along radar lines of sight and the input v_{los} for the full day of 26 March 2014.

7. Summary and Conclusions

This paper presents a new technique for estimation of the global-scale convection pattern in the ionosphere. The technique evolved from the ideas originally applied in localized regions to examine convection structure (Bristow et al., 2016). The technique applies Bayesian inverse theory to derive the plasma velocity at every point in the domain of consideration based upon the v_{los} observed by the SuperDARN radars combined with a machine-learning based climatological model of convection and applying the assumption that the velocity field is divergence free. The resulting velocity field forms a coherent pattern that exhibits structure at scales of less than 100 km.

The computer code for the technique has the ability to include a region with a higher spatial resolution than is used in the full domain. In the examples presented, the main grid used grid cells that were about 100 × 100 km and a nested region with cells that were about 50 × 50 km. Higher resolutions are possible if higher resolution input observations are available.

In the example patterns shown, there is a close correspondence between the features of the plasma velocity and observations of the aurora. One particular example shows a brief interval with high-speed poleward flows in a localized region accompanied by rapid poleward motion of the aurora. The high-speed flow began and ceased at the same time as the poleward motion of the arcs, and had an average velocity that was about the same as an estimate of the arc velocity based on their displacement divided by the time over which they moved.

The electrostatic potential can be estimated through integration of the electric fields obtained from the plasma velocities under the assumption that they result from the E-cross-B drift. The resulting patterns can be used to drive global circulation models of the ionosphere and theromosphere if they have the ability to ingest the high-resolution grid. This ability will be critical to examining the impacts of small-scale convection features on global geospace.

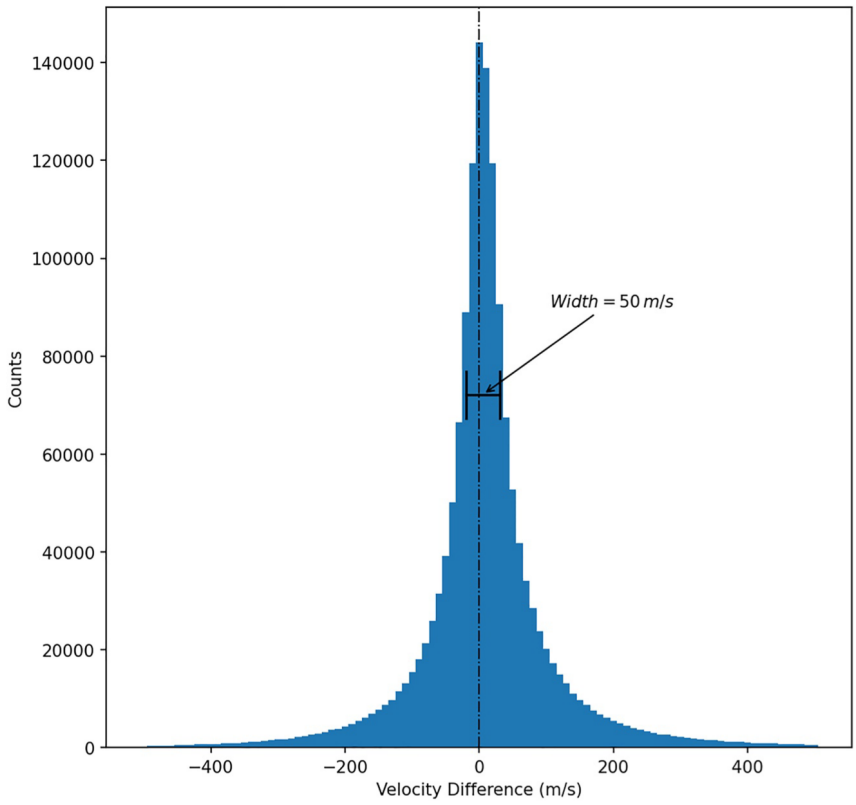

Figure 10. Distribution of differences between the projections of velocities along radar lines of sight and the input v_{los} for the full day of 26 March 2014.

Appendix A: Velocity Divergence When Ion-Neutral Collisions Are Present

If it is assumed that the electrons remain frozen to the field lines then the Pedersen current is due to ion motion in the direction of **E**. The F-region ion momentum equation ignoring pressure gradients, inertia, and motion of the neutral gas can be written as follows:

$$\mathbf{E} + \mathbf{v} \times \mathbf{B} = \frac{m\nu}{q}\mathbf{v} \tag{A1}$$

where m is the F-region ion mass, q is the ion charge, and ν is the ion-neutral collision frequency. Choosing a coordinate system with the z-axis parallel to the local **B**, Equation A1 can be written as follows:

$$\mathbf{E} + \begin{bmatrix} 0 & B_z \\ -B_z & 0 \end{bmatrix}\mathbf{v} - \begin{bmatrix} \frac{m\nu}{q} & 0 \\ 0 & \frac{m\nu}{q} \end{bmatrix}\mathbf{v} = 0 \tag{A2}$$

Defining β and solving for **v**:

$$\beta = \begin{bmatrix} -\frac{m\nu}{q} & \frac{m\Omega}{q} \\ \frac{m\Omega}{q} & -\frac{m\nu}{q} \end{bmatrix} \qquad \Rightarrow \qquad \mathbf{v} = \boldsymbol{\beta}^{-1}\mathbf{E} \tag{A3}$$

where magnitude of B has been replaced with the ion gyrofrequency multiplied by mass over charge ($B_z = m\Omega/q$), and $\boldsymbol{\beta}^{-1}$ is as follows:

$$\boldsymbol{\beta}^{-1} = \frac{q}{m\nu}\begin{bmatrix} \frac{\nu^2}{\nu^2+\Omega^2} & \frac{\Omega\nu}{\nu^2+\Omega^2} \\ \frac{-\Omega\nu}{\nu^2+\Omega^2} & \frac{\nu^2}{\nu^2+\Omega^2} \end{bmatrix} \tag{A4}$$

The leading coefficient, $q/m\nu$, is the mobility of ions parallel to the magnetic field. Assuming the quantities in β are constant in the direction perpendicular to **B**, the divergence of Equation A3 yields the following equation:

$$\nabla \cdot \mathbf{v} = \frac{1}{\nu^2/\Omega^2 + 1} \nabla \cdot \left(\mathbf{E} \times \mathbf{B}/B^2 \right) + \frac{q\nu/m}{\nu^2 + \Omega^2} \nabla \cdot \mathbf{E} \quad \text{(A5)}$$

Data Availability Statement

The rawacf data used in this study were processed using standard SuperDARN FitACF version 3 algorithm from the SuperDARN Radar Software Toolkit Version 4.6 (https://github.com/SuperDARN/rst-archive/tree/rst.4.6). The raw SuperDARN data are available from the British Antarctic Survey (BAS) SuperDARN data server (https://www.bas.ac.uk/project/superdarn) or one of the other SuperDARN data mirrors. The IMF, solar wind, and geomagnetic index data are available from the NASA Space Physics Data Facility OMNIWeb data server (https://omniweb.gsfc.nasa.gov/) THEMIS all-sky imager data were pulled from http://themis.ssl.berkeley.edu/themisdata//thg/l1/asi/. A code that implements the G-LDFF is available through GitHub at the URLs https://github.com/wab5217-psu/Global_LDFF and https://github.com/wab5217-psu/GLDFF_Potential. The machine-learning convection model file needed to reproduce the plots in this study can be found at https://zenodo.org/record/7182724.

Acknowledgments
SuperDARN operations and research at Pennsylvania State University are supported under NSF Grants PLR-1443504 from the Office of Polar Programs and AGS-1934419 from the Geospace Section of NSF Division of Atmospheric and Geospace Sciences. The authors acknowledge the use of SuperDARN data. SuperDARN is a collection of radars funded by national scientific funding agencies of Australia, Canada, China, France, Italy, Japan, Norway, South Africa, United Kingdom, and the United States of America. We acknowledge use of NASA/GSFC's Space Physics Data Facility's OMNIWeb service and OMNI data. Work at UCLA has been supported by NSF Grant 2055192 and AFOSR FA9559-16-1-0364. Work at Boston University was supported by NASA Grants 80NSSC18K0657, 80NSSC20K0604, 80NSSC20K0725, 80NSSC21K1321, and 80NSSC19K0546, NSF Grant AGS-1907698 and AGS-2100975, and AFOSR Grant FA9559-16-1-0364. The authors thank the Canadian Space Agency for financial support of the operations of the THEMIS-ASI network, and the University of California Berkeley and University of Calgary THEMIS-ASI teams for maintaining THEMIS-ASI and making the data available. The THEMIS mission is supported by NASA NAS5-02099 and Canada Foundation for Innovation. SuperDARN operations and research at Dartmouth College are supported by NSF Grant AGS-1934997.

References

Bristow, W. A., Hampton, D. L., & Otto, A. (2016). High-spatial-resolution velocity measurements derived using local divergence-free fitting of superdarn observations. *Journal of Geophysical Research: Space Physics*, *121*(2), 1349–1361. https://doi.org/10.1002/2015JA021862

Bristow, W. A., Topliff, C. T., & Cohen, M. B. (2022). Development of a high-latitude convection model by application of machine learning to superdarn observations. *Space Weather*, *121*(2), 1349–1361. https://doi.org/10.1002/2015JA021862

Burke, W., Hardy, D., Rich, F., Kelley, M., Smiddy, M., Shuman, B., et al. (1980). Electrodynamic structure of the late evening sector of the auroral zone. *Journal of Geophysical Research*, *85*(A3), 1179–1193. https://doi.org/10.1029/JA085iA03p01179

Chisham, G., Lester, M., Milan, S. E., Freeman, M. P., Bristow, W. A., Grocott, A., et al. (2007). A decade of the super dual auroral radar network (SuperDARN): Scientific achievements, new techniques and future directions. *Surveys in Geophysics*, *28*(1), 33–109. https://doi.org/10.1007/s10712-007-9017-8

Cousins, E. D. P., Matsuo, T., & Richmond, A. D. (2013a). Mesoscale and large-scale variability in high-latitude ionospheric convection: Dominant modes and spatial/temporal coherence. *Journal of Geophysical Research: Space Physics*, *118*(12), 7895–7904. https://doi.org/10.1002/2013JA019319

Cousins, E. D. P., Matsuo, T., & Richmond, A. D. (2013b). Superdarn assimilative mapping. *Journal of Geophysical Research: Space Physics*, *118*(12), 7954–7962. https://doi.org/10.1002/2013JA019321

Cousins, E. D. P., & Shepherd, S. G. (2010). A dynamical model of high-latitude convection derived from superdarn plasma drift measurements. *Journal of Geophysical Research*, *115*(A12), A12329. https://doi.org/10.1029/2010JA016017

Gallardo-Lacourt, B., Nishimura, Y., Lyons, L. R., Zou, S., Angelopoulos, V., Donovan, E., et al. (2014). Coordinated SuperDARN THEMIS ASI observations of mesoscale flow bursts associated with auroral streamers. *Journal of Geophysical Research: Space Physics*, *119*(1), 142–150. https://doi.org/10.1002/2013JA019245

Greenwald, R. A., Baker, K. B., Dudeney, J. R., Pinnock, M., Jones, T. B., Thomas, E. C., et al. (1995). DARN/SuperDARN: A global view of high-latitude convection. *Space Science Reviews*, *71*(1–4), 763–796. https://doi.org/10.1007/bf00751350

Greenwald, R. A., Baker, K. B., Hutchins, R. A., & Hanuise, C. (1985). An hf phased-array radar for studying small-scale structure in the high-latitude ionosphere. *Radio Science*, *20*(1), 63–79. https://doi.org/10.1029/RS020i001p00063

Heppner, J. P., & Maynard, N. C. (1987). Empirical high-latitude electric field models. *Journal of Geophysical Research*, *92*(A5), 4467–4489. https://doi.org/10.1029/JA092iA05p04467

Hestenes, M. R., & Stiefel, E. (1952). Methods of conjugate gradients for solving linear systems. *Journal of Research of the National Bureau of Standards*, *49*(6), 409–436. https://doi.org/10.6028/jres.049.044

Kamide, Y., Richmond, A. D., & Matsushita, S. (1981). Estimation of ionospheric electric fields, ionospheric currents, and field-aligned currents from ground magnetic records. *Journal of Geophysical Research*, *86*(A2), 801–813. https://doi.org/10.1029/JA086iA02p00801

King, J. H., & Papitashvili, N. E. (2005). Solar wind spatial scales in and comparisons of hourly wind and ace plasma and magnetic field data. *Journal of Geophysical Research*, *110*(A2), A02104. https://doi.org/10.1029/2004JA010649

Kivelson, M. G., & Southwood, D. J. (1991). Ionospheric signatures of localized magnetospheric perturbations. *Journal of Geomagnetism and Geoelectricity*, *43*(1), 129–140. https://doi.org/10.5636/jgg.43.Supplement1_129

Lockwood, M., & Morley, S. K. (2004). A numerical model of the ionospheric signatures of time-varying magneticreconnection: I. Ionospheric convection. *Annales Geophysicae*, *22*(1), 73–91. https://doi.org/10.5194/angeo-22-73-2004

Lyons, L. R., Gallardo-Lacourt, B., & Nishimura, Y. (2022). Chapter 2—Auroral structures: Revealing the importance of meso-scale MI coupling. In Y. Nishimura, O. Verkhoglyadova, Y. Deng, & S.-R. Zhang (Eds.), *Cross-scale coupling and energy transfer in the magnetosphere-ionosphere-thermosphere system* (pp. 65–101). Elsevier. https://doi.org/10.1016/B978-0-12-821366-7.00004-4

Lyons, L. R., Nishimura, Y., Zhang, S.-R., Coster, A. J., Bhatt, A., Kendall, E., & Deng, Y. (2019). Identification of auroral zone activity driving large-scale traveling ionospheric disturbances. *Journal of Geophysical Research: Space Physics*, *124*(1), 700–714. https://doi.org/10.1029/2018JA025980

Lysak, R. L. (1985). Auroral electrodynamics with current and voltage generators. *Journal of Geophysical Research*, *90*(A5), 4178–4190. https://doi.org/10.1029/JA090iA05p04178

Matsuo, T., Fan, M., Shi, X., Miller, C., Ruohoniemi, J. M., Paul, D., & Lee, T. C. M. (2021). Multiresolution modeling of high-latitude ionospheric electric field variability and impact on joule heating using superdarn data. *Journal of Geophysical Research: Space Physics*, *126*(9), e2021JA029196. https://doi.org/10.1029/2021JA029196

Matsuo, T., Richmond, A. D., & Lu, G. (2005). Optimal interpolation analysis of high-latitude ionospheric electrodynamics using empirical orthogonal functions: Estimation of dominant modes of variability and temporal scales of large-scale electric fields. *Journal of Geophysical Research*, *110*(A6), A06301. https://doi.org/10.1029/2004JA010531

Nishitani, N., Ruohoniemi, J. M., Lester, M., Baker, J. B. H., Koustov, A. V., Shepherd, S. G., et al. (2019). Review of the accomplishments of mid-latitude super dual auroral radar network (superdarn) HF radars. *Progress in Earth and Planetary Science*, *6*(1), 27. https://doi.org/10.1186/s40645-019-0270-5

Papitashvili, V. O., Belov, B. A., Faermark, D. S., Feldstein, Y. I., Golyshev, S. A., Gromova, L. I., & Levitin, A. E. (1994). Electric potential patterns in the northern and southern polar regions parameterized by the interplanetary magnetic field. *Journal of Geophysical Research*, *99*(A7), 13251–13262. https://doi.org/10.1029/94JA00822

Pettigrew, E. D., Shepherd, S. G., & Ruohoniemi, J. M. (2010). Climatological patterns of high-latitude convection in the northern and southern hemispheres: Dipole tilt dependencies and interhemispheric comparisons. *Journal of Geophysical Research*, *115*(A7), A07305. https://doi.org/10.1029/2009JA014956

Richmond, A. D. (1992). Assimilative mapping of ionospheric electrodynamics. *Advances in Space Research*, *12*(6), 59–68. https://doi.org/10.1016/0273-1177(92)90040-5

Richmond, A. D., & Kamide, Y. (1988). Mapping electrodynamic features of the high-latitude ionosphere from localized observations: Technique. *Journal of Geophysical Research*, *93*(A6), 5741–5759. https://doi.org/10.1029/JA093iA06p05741

Ridley, A. J., Deng, Y., & Tóth, G. (2006). The global ionosphere thermosphere model. *Journal of Atmospheric and Solar-Terrestrial Physics*, *68*(8), 839–864. https://doi.org/10.1016/j.jastp.2006.01.008

Roble, R. G., & Ridley, E. C. (1994). A thermosphere-ionosphere-mesosphere-electrodynamics general circulation model (TIME-GCM): Equinox solar cycle minimum simulations (30–500 km). *Geophysical Research Letters*, *21*(6), 417–420. https://doi.org/10.1029/93GL03391

Ruohoniemi, J. M., & Baker, K. B. (1998). Large-scale imaging of high-latitude convection with super dual auroral radar network HF radar observations. *Journal of Geophysical Research*, *103*(20), 797–20811. https://doi.org/10.1029/98ja01288

Ruohoniemi, J. M., & Greenwald, R. A. (1996). Statistical patterns of high-latitude convection obtained from goose bay HF radar observations. *Journal of Geophysical Research*, *101*(A10), 21743–21763. https://doi.org/10.1029/96JA01584

Sangalli, L., Knudsen, D. J., Larsen, M. F., Zhan, T., Pfaff, R. F., & Rowland, D. (2009). Rocket-based measurements of ion velocity, neutral wind, and electric field in the collisional transition region of the auroral ionosphere. *Journal of Geophysical Research*, *114*(A4), A04306. https://doi.org/10.1029/2008JA013757

Shepherd, S. G. (2014). Altitude-adjusted corrected geomagnetic coordinates: Definition and functional approximations. *Journal of Geophysical Research: Space Physics*, *119*(9), 7501–7521. https://doi.org/10.1002/2014JA020264

Shepherd, S. G., & Ruohoniemi, J. M. (2000). Electrostatic potential patterns in the high-latitude ionosphere constrained by SuperDARN measurements. *Journal of Geophysical Research*, *105*(A10), 23005–23014. https://doi.org/10.1029/2000JA000171

Thomas, E. G., & Shepherd, S. G. (2018). Statistical patterns of ionospheric convection derived from mid-latitude, high-latitude, and polar SuperDARN HF radar observations. *Journal of Geophysical Research: Space Physics*, *123*(4), 3196–3216. https://doi.org/10.1002/2018JA025280